RSC Advances

PAPER

View Article Online
View Journal | View Issue

Cite this: *RSC Adv.*, 2025, **15**, 27345

Comparative study of Ta and Ga doping effects on $Li_7La_3Zr_2O_{12}$ garnet electrolytes for advanced thermal battery applications†

Hyungu Kang,[a] Heesook Roh,[a] Jongseo Lee,[a] Sang-Hyeon Park,[a] Joohyeon Park,[b] Heonjae Jeong,[bc] Hyun-Ki Yoon,[a] Tae-Young Ahn *[a] and Yusong Choi *[a]

The paradigm shift from conventional molten-salt electrolytes to solid-state garnet-type $Li_7La_3Zr_2O_{12}$ (LLZO) electrolytes in thermal batteries represents a critical advancement in high-temperature energy-storage systems. This study evaluated Ta- and Ga-doped LLZO electrolytes for FeS_2/Li–Si thermal batteries, focusing on their structural stability and electrochemical performance at 500 °C. While Ga-doped LLZO exhibited superior ionic conductivity at 25 °C, Ta-doped LLZO demonstrated exceptional high-temperature stability. Ta-doped LLZO cells achieved longer discharge durations and higher energy densities than Ga-doped LLZO cells, which is attributed to the retained cubic phase and minimised interfacial degradation. Conversely, Ga-doped LLZO exhibited cubic-to-tetragonal phase transitions, Ga precipitation, and formation of impurities such as Ga_2O_3 and Li–Ga alloys, leading to 54% loss of ionic conductivity post-discharge. These results contribute valuable insights for the optimisation of solid-state electrolytes in thermal battery systems, suggesting that conventional room-temperature performance metrics may not translate directly to elevated-temperature operations.

Received 3rd June 2025
Accepted 23rd July 2025

DOI: 10.1039/d5ra03917g

rsc.li/rsc-advances

1. Introduction

Thermal batteries, often classified as reserve batteries, are critical power sources for military and aerospace applications owing to their long shelf life (>10 years) and instantaneous activation at elevated temperatures (350–550 °C).[1] To accommodate the increasing power demands of advanced military equipment, thermal batteries require large-diameter electrodes and electrolytes. These systems traditionally employ molten-salt electrolytes (*e.g.* LiCl–KCl (LK) and LiF–LiCl–LiBr eutectic) that solidify at room temperature, thereby eliminating self-discharge because of their nonconductive nature in the solid state. At operating temperatures, the molten-salt electrolyte liquefies, facilitating high-powder discharge owing to its high intrinsic ionic conductivity (1850 mS cm^{-1} for LK at 500 °C).[1] However, in practical applications, the overflow of molten salts caused by volumetric expansion remains a significant obstacle to the use of thermal batteries.[2] Although the incorporation of binder additives such as MgO or SiO_2 has been proposed to mitigate this issue, the risk of short circuits due to salt leakage persists.[2–4] This phenomenon is exacerbated in high-vibration environments (*e.g.* rotating munitions). Therefore, to enhance performance and stability, strategies for integrating solid electrolytes into thermal batteries to fundamentally eliminate the issue of molten-salt leakage must be developed.

When replacing molten salts with solid electrolytes, the material selection must balance ionic conductivity, thermal stability, and interfacial compatibility. Sulfide-based electrolytes (*e.g.* $Li_{10}GeP_2S_{12}$) are known for their ultrahigh ionic conductivity (>10 mS cm^{-1} at 25 °C); however, their poor thermal stability and reactivity with Li anodes limit their high-temperature applications.[5–7] Polymer electrolytes, *e.g.* polyethylene oxide–polytetrafluoroethylene composites, offer mechanical flexibility and processability but suffer from decomposition above 200 °C.[8,9] Oxide electrolytes, *e.g.* $Li_{0.33}LaTiO_3$ and $Li_{1.3}Al_{0.3}Ti_{1.7}(PO_4)_3$, provide moderate conductivity and thermal resilience but face challenges such as reactivity with Li anodes.[10,11]

Garnet-type $Li_7La_3Zr_2O_{12}$ (LLZO) has emerged as a promising alternative as it offers competitive Li^+ ionic conductivity, broad electrochemical stability (>5.5 V *vs.* Li/Li^+), and structural robustness at high temperatures.[12–16] Furthermore, in contrast to sulfides and polymers, the use of LLZO eliminates toxic byproducts, making it uniquely suited for thermal battery systems requiring both safety and high performance at extreme temperatures. Native LLZO exists in a tetragonal phase (space group $I4_1/acd$) at room temperature, characterised by ordered Li^+ sublattices and poor ionic conductivity (~10^{-6} S cm^{-1}). At

[a]*Defense Materials and Energy Development Center, Agency for Defense Development, Yuseong P.O. Box 35, Daejeon, 34060, South Korea. E-mail: tyahn84@gmail.com; richpine87@gmail.com; Tel: +82-42-821-3520; +82-42-821-2457*

[b]*Department of Electronic Engineering, Gachon University, 1342 Seongnam-daero, Seongnam, Gyeonggi 13120, South Korea*

[c]*Department of Semiconductor Engineering, Gachon University, 1342 Seongnam-daero, Seongnam, Gyeonggi 13120, South Korea*

† Electronic supplementary information (ESI) available. See DOI: https://doi.org/10.1039/d5ra03917g

elevated temperatures (~650 °C), it transitions to a cubic phase (space group $Ia\bar{3}d$), where a disordered Li^+ distribution enables significantly increases the conductivity (>10^{-4} S cm^{-1}).[15,17] This phase transition underscores the potential of the material in battery applications but necessitates doping strategies to stabilise the cubic phase.

Aliovalent doping (*e.g.* Ta^{5+}, Ga^{3+}) at Zr^{4+} or Li^+ sites introduces Li^+ vacancies and adjustments in Li^+ transmission pathways with regulation of the lattice parameters, disrupting Li ordering and lowering the cubic-phase stabilisation temperature.[12,18–24] Among these, Ga-doped LLZO (Ga-LLZO) has demonstrated superior efficacy, displaying room-temperature ionic conductivity of ~2×10^{-3} S cm^{-1}.[25,26] Ga^{3+} is substituted directly onto Li^+ sites, which creates two vacancies on adjacent Li^+ sites and disorder in the crystal lattice to maintain charge balance.[12,23,27] This creates additional Li^+ ion channels such as the 96h → 96h migration path.[28] Moreover, compared with other dopants, the diminished coulombic repulsion between Ga^{3+} and Li^+ ions lowers the energy barrier for localised Li^+ diffusion, promoting efficient percolation of Li^+ across extended lattice networks.[27]

In this study, we systematically evaluated Ta-doped LLZO (Ta-LLZO) and Ga-LLZO electrolytes in FeS_2/Li–Si thermal batteries, focusing on their structural evolution, ionic transport, and discharge performance at 500 °C. By integrating experimental and computational methods, we demonstrated how dopant chemistry governs phase stability and interfacial reactions. Our findings challenge conventional electrolyte selection criteria by demonstrating that room-temperature conductivity metrics are unable to accurately predict high-temperature performance, emphasising the need for operational-condition-specific material design.

2. Experimental section

2.1. Thermal battery unit cell assembly and discharge testing

The unit cells used in discharge tests composed cathode, electrolyte, and anode disks. Owing to the moisture sensitivity of thermal battery components, all manufacturing, storage, and testing procedures were conducted in a controlled dry room with regulated atmospheric moisture.

$Ta_{0.5}$ and $Ga_{0.2}$ were selected as the dopant concentrations for LLZO according to previous reports indicating optimal ionic conductivity at these compositions. For Ta-LLZO, studies have demonstrated that $Li_{6.5}La_3Zr_{1.5}Ta_{0.5}O_{12}$ ($Ta_{0.5}$-LLZO) has high conductivity (>1×10^{-3} S cm^{-1}) owing to its increased Li^+ vacancy concentration and lattice stability.[19,20] Similarly, $Li_{6.4}Ga_{0.2}La_3Zr_2O_{12}$ ($Ga_{0.2}$-LLZO) achieves ionic conductivities above 1×10^{-3} S cm^{-1} by balancing Li^+ vacancy formation.[22,23,29] Sharifi *et al.*[21] achieved a high ionic conductivity of 5.85×10^{-3} S cm^{-1} at 20 °C using a sol–gel combustion process. In the present study, the consistent use of $Ta_{0.5}$-LLZO and $Ga_{0.2}$-LLZO across all experiments ensured a direct, literature-supported comparison of dopant effects, as these concentrations are widely recognised as the concentrations for achieving optimal ionic conductivity in their respective systems.

LiCl (Vitzrocell Co., Ltd) and KCl (DUKSAN HIGHCHEM CORP.) powders were separately vacuum-dried and then mixed in eutectic proportions. The LK salt mixture was subsequently melted under an Ar atmosphere and mixed with MgO (Sigma-Aldrich). The cathode material was prepared by mixing FeS_2 powder (Sigma-Aldrich) with the LK salt/MgO mixture and Li_2O (DUKSAN HIGHCHEM CORP). For the anode, the LK salt/MgO mixture was combined with an Li–Si alloy (Gelon Energy Corp). The electrolyte preparation began by mixing the LK salt mixture with doped LLZO powder (POSCO JK Solid Solution, Pohang, Korea) in a mass ratio of 25 : 75, which was essential to improve formability and facilitate large-scale processing, as cold pressing of pure LLZO presents challenges in fabricating large-diameter pellets. The cathode, anode, and electrolyte mixture powder were placed in a 56 mm-diameter mould and uniaxially pressed to form a circular disk. These components were then assembled to form the complete thermal battery unit cell with current collectors (STS304) and used in subsequent electrochemical testing and performance evaluation.

Discharge tests were conducted under controlled conditions to evaluate the electrochemical performance of the fabricated thermal battery unit cells. To minimise the contact resistance between components, the cells were placed in a press and subjected to a constant applied force of 250 kgf throughout the testing process. Prior to testing, the batteries were heated to 500 °C and allowed to stabilise for at least 10 min to ensure uniform temperature and complete melting of the LK salt, increasing the ionic conductivity. To evaluate the internal resistance of the thermal battery, pulse discharge tests were conducted under two distinct current-density conditions: 0.1 A_{avg} cm^{-2} (low) and 0.5 A_{avg} cm^{-2} (high). For the low-current-density discharge, pulse sequences consisted of a 2.45 A constant current for 8 s, followed by 0 A for 1 s and then 4.9 A for 1 s. Similarly, 12.25 A (8 s), 0 A (1 s), and 24.5 A (1 s) cycles were applied for high-current-density pulse testing. The voltage profile was recorded using a potentiostat/galvanostat system equipped with high-temperature-compatible probes.

2.2. Electrochemical impedance spectroscopy measurements

Ta- and Ga-LLZO pellets were fabricated for electrochemical impedance spectroscopy (EIS) analysis by uniaxially pressing doped LLZO powder in a 13 mm-diameter mould under a pressure of 250 MPa, resulting in pellets with a thickness of approximately 1.5 mm. The pressed pellets were then sintered at 1200 °C for 4 h in a furnace under an Ar atmosphere to achieve densification. The pellet surfaces were polished to ensure flatness, followed by the deposition of Pt electrodes on both sides using a magnetron sputter coater (Sputter Coater 108, Cressington) to achieve reliable electrical contact.

To examine the influence of the Li–Si alloy on doped LLZO at elevated temperatures, Li–Si pellets with identical dimensions were fabricated *via* uniaxial pressing. The experimental setup comprised a Li–Si pellet placed beneath both Ta-LLZO and Ga-LLZO pellets in a stacked configuration. This assembly was

placed in an Ar-controlled glovebox containing a furnace, where the two stacks were heated at 500 °C for 5 h.

Impedance measurements were performed using a high-temperature ion conductivity measurement system (TPU-005N, TeraLeader) capable of simultaneous pressure application and thermal control. Pellets were placed in a ceramic insulator and subjected to a constant pressure of 150 kgf during testing. Electrochemical impedance spectra were acquired using a BioLogic SP-50e potentiostat over the frequency range of 100 Hz to 1 MHz with an alternating-current (AC) voltage amplitude of 100 mV. Measurements were peformed from 25 to 100 °C, and the acquired impedance data were fitted using ZFit software (BioLogic) to extract resistance values from Nyquist plots.

2.3. Microstructural observation

The chemical compositions and microstructures of LLZO pellets and thermal battery unit cells were characterised using scanning electron microscopy (SEM; FEI-QUANTA650) with energy-dispersive X-ray spectroscopy (EDS). Uniaxial pressing was performed to prepare the sample for SEM imaging, and the surface was polished to achieve flatness prior to EDS analysis.

2.4. X-ray diffraction analysis

X-ray diffraction (XRD) analysis was performed using a SmartLab X-ray diffractometer (Rigaku, Cu Kα radiation source). *In situ* XRD measurements were taken under a He atmosphere to minimise interfacial reaction between the sample and environmental components such as moisture or atmospheric gases. The samples were thermally stabilised at three critical temperatures—room temperature (25 °C), 300 °C, and 500 °C—by maintaining them at these temperatures for at least 1 h. Diffraction data were acquired using a scan speed of 2° min^{-1} and a step size of 0.01°. After the high-temperature measurements were complete, the samples were gradually cooled back to room temperature, and a final XRD scan was performed to assess the phase stability and structural reversibility.

2.5. Differential scanning calorimetry analysis

Differential scanning calorimetry (DSC) measurements were performed using a Parr 6100EF Calorimeter (Parr Instrument Company) housed in a moisture-controlled dry room to ensure environmental stability. Samples were analysed from room temperature (25 °C) to 580 °C to investigate the heat-flow characteristics and thermal transitions.

2.6. Computational methods

First-principles density functional theory (DFT) and *ab initio* molecular dynamic (AIMD) simulations were performed using the Vienna *Ab initio* Simulation Package (VASP).[30] The projector augmented wave method[31] and Perdew–Burke–Ernzerhof[32] generalised gradient approximation exchange-correlation functional were used. A plane-wave cutoff energy of 520 eV was applied, and 2 × 2 × 2 and 2 × 2 × 1 Monkhorst–Pack *k*-point grids[33] were adopted for bulk and slab calculations, respectively. We set the surface termination according to the lowest surface energy among the low Miller indices, particularly LLZO(100), while $Li_{13}Si_4$(011) was selected due to its favorable lattice matching and larger interfacial contact area with LLZO(100), despite not being the lowest energy surface.

We modelled an interface between LLZO(100) and $Li_{13}Si_4$(011) using VASPKIT,[34] where the interfacial area was 25.2 × 18.0 $Å^2$ with a total thickness of 36.4 Å and vacuum length of 10.0 Å. The interfacial gap was separated by 3.0 Å, and the lattice mismatch was 5.5%.

For AIMD simulations, owing to high computational demands, a reduced plane-wave cutoff energy of 400 eV was used, and the Brillouin zone was sampled only at the gamma point. AIMD simulations were conducted for 1 ps with a time-step of 1 fs, employing a Nosé–Hoover thermostat and a canonical ensemble (NVT) at 773 K.

To investigate the tendency of dopant precipitation from the doped LLZO, we calculated the defect formation energy (DFE). The precipitation sites of the dopant (Ta or Ga) were selected according to the lowest DFE value. The DFE is given by[35]

$$\mathrm{DFE} = E_{\mathrm{defect}} - E_{\mathrm{pristine}} + \mu_{\mathrm{defect}}, \quad (1)$$

where E_{defect} and E_{pristine} denote the total energies of the doped LLZO structure in the absence and presence of a dopant, respectively. Moreover, μ_{defect} represents the chemical potential of the defect (dopant) species and is a function of temperature (T) and pressure (P). However, P is negligible in solids; therefore, μ_{defect} is computed as

$$\mu_{\mathrm{defect}} = \mu_{\mathrm{defect}}^{\mathrm{DFT}} + \Delta\mu(T), \quad (2)$$

where $\mu_{\mathrm{defect}}^{\mathrm{DFT}}$ represents the total energy calculated using DFT and $\Delta\mu(T)$ is the temperature correction term, which is given as

$$\Delta\mu(T) = \Delta H(T) - T\Delta S(T). \quad (3)$$

here, enthalpy (H) and entropy (S) were obtained from the standard thermodynamic tables.[36] At T = 773 K, $\Delta\mu_{\mathrm{Ga}}$ is −0.43 eV per atom, and $\Delta\mu_{\mathrm{Ta}}$ is −0.34 eV per atom. The calculation details are presented in Table S1.†

The DFE represents the thermodynamic stability of Ta and Ga dopants, indicating their tendency either to remain incorporated within the system or to be released. Lower DFE values correspond to a higher likelihood of dopant annihilation (precipitation) from LLZO, whereas higher values reflect enhanced stability in LLZO. Negative DFE values suggest that dopant release is thermodynamically favourable and can spontaneously occur. To compare the favourable regions, the DFEs were calculated for both bulk and interface structures. To provide thermal perturbation on structural relaxation, structures were obtained from AIMD simulations at an elevated temperature of 773 K.

3. Results and discussion

3.1. Structural and electrochemical validation of doped LLZO garnet electrolytes

Fig. 1(a) presents the room-temperature XRD patterns of undoped, Ta-LLZO, and Ga-LLZO electrolytes prepared *via*

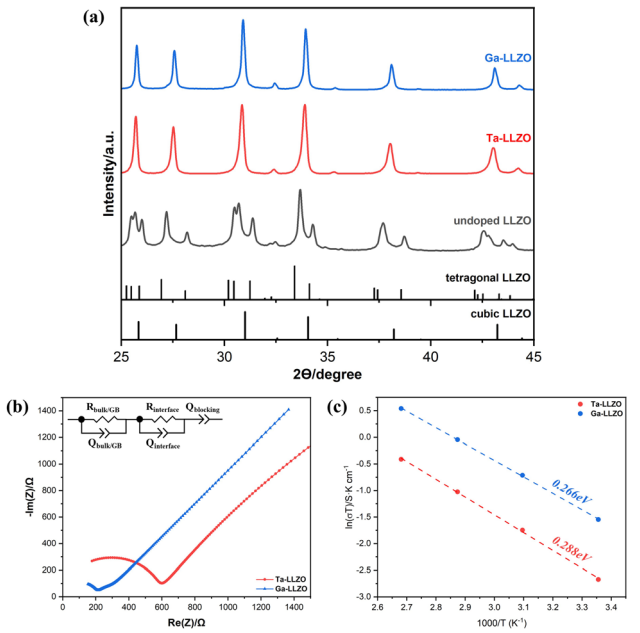

Fig. 1 (a) XRD patterns of undoped, Ta-doped, and Ga-doped LLZO powders; (b) Nyquist plots of Ta- and Ga-doped LLZO pellets at room temperature (25 °C); (c) Arrhenius plots of total conductivities for Ta- and Ga-doped LLZO pellets at temperatures of 25, 50, 75, and 100 °C.

conventional solid-state synthesis, alongside reference patterns for cubic and tetragonal LLZO phases. The undoped LLZO clearly exhibits a tetragonal structure (space group $I4_1/acd$), which is consistent with its thermodynamic stability under ambient conditions, whereas the doped variants successfully transformed into the cubic phase (space group $Ia\bar{3}d$), confirming effective dopant incorporation into the LLZO lattice. Impurities such as $La_2Zr_2O_7$ or Li_2ZrO_3, which are frequently reported in LLZO synthesis, were not detected in any of the samples.[15,23,26,37]

Fig. 1(b) shows the Nyquist plots for Ta- and Ga-LLZO pellets, obtained at 25 °C after uniaxial pressing. The impedance spectra typically show two semicircles in the high- and intermediate-frequency regions, followed by a long diagonal tail in the low-frequency domain. Each semicircle corresponds to a parallel combination of resistance and constant-phase elements in the equivalent circuit model. While studies have suggested that the two semicircles correspond to the bulk and grain-boundary components,[26,38,39] other reports have indicated that these features in the Nyquist plot cannot be easily separated.[40–43] Therefore, the first semicircle in the high-frequency region is assigned to the combined resistance of bulk and grain-boundary components, representing the total solid electrolyte resistance. The second semicircle is attributed to the interfacial resistance between the solid electrolyte pellet and electrodes.[41–43] The low-frequency tail represents the blocking effect resulting from the use of Pt electrodes, where ions accumulate at the electrode surface and cannot pass through, leading to increased double-layer capacitance.[40,43–45] Therefore, the experimental data were analysed using an equivalent circuit model of $(R_{bulk/GB}Q_{bulk/GB})(R_{interface}Q_{interface})Q_{blocking}$ to calculate the solid electrolyte resistance.[46–48] The total conductivity (σ_{total}) was calculated using the thickness (t) and area (A) of the LLZO pellet: $\sigma_{total} = t/(AR_{bulk/GB})$. The room-temperature ionic conductivities calculated using the total solid electrolyte resistance were 2.32×10^{-4} and 7.14×10^{-4} S cm^{-1} for Ta- and Ga-LLZO, respectively, which are consistent with previously reported findings.[23,27,28,49]

Moreover, EIS measurements were conducted at 50, 75, and 100 °C, and the results are presented as an Arrhenius plot in Fig. 1(c). The calculated activation energies were 0.288 and 0.266 eV for Ta- and Ga-LLZO, respectively, with the values falling within the typical range (0.20–0.40 eV) that has been reported for doped LLZO materials.[23,27,28,49] The lower activation energy of Ga-LLZO may reflect its superior ionic conductivity compared with that of Ta-LLZO, as a reduced activation energy signifies lower energy barriers for Li^+ migration. The temperature-dependent Nyquist plots for each composition are shown in Fig. S1.† According to both previous studies and our investigation, the room-temperature ionic conductivity of doped LLZO follows the trend of Ga-LLZO > Ta-LLZO.[23,25–27,49]

3.2. Discharge performance of Ta- and Ga-LLZO electrolytes in FeS_2/Li–Si thermal batteries

The discharge characteristics were evaluated to determine the effect of dopant type on battery performance at elevated temperatures. While the main objective of this study was to fully replace the molten-salt electrolyte with LLZO, 25 wt% of eutectic LK was included in the electrolyte disk in this study to ensure adequate electrochemical performance under high-temperature discharge conditions. Given that all the cell materials and experimental conditions remained identical across the tests except for the type of dopant, the differences in discharge performance are attributed solely to the variation in electrolyte dopant species.

Fig. 2(a) and (b) illustrate the discharge profiles at constant current densities of 0.1 and 0.5 A_{avg} cm^{-2}, respectively. Following the initial discharge period, repeated pulse patterns were applied to evaluate the dynamic response characteristics of the cells. Both cells exhibited polarisation phenomena during these rapid current transitions, with the voltage unable to fully respond to the abrupt current changes. The delayed voltage recovery may have resulted from the inability of Li ions in the solid electrolyte to reach the electrode surface with sufficient speed to sustain the electrode reactions.[50,51]

The open-circuit voltage (OCV) recorded immediately before discharge was approximately 1.92 V for every discharge test. This aligns well with previous reports presenting similar values for thermal batteries employing FeS_2 cathodes and Li–Si alloy anodes at a discharge temperature of 500 °C.[52–55] During discharge, three distinct voltage plateaus were observed for both cells. This multi-plateau behaviour has been extensively documented in previous research on Li–Si electrochemistry during Li–Si alloy delithiation.[56–60] The phase transitions in Li–Si alloys at discharge typically develop a series of reactions involving the formation of intermediate phases as follows:

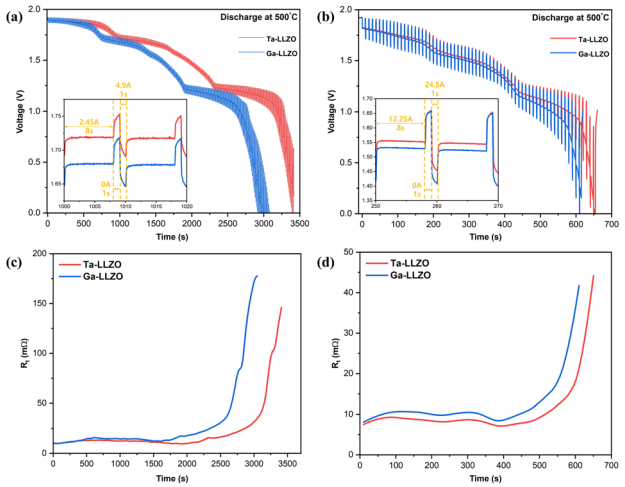

Fig. 2 Thermal battery discharge test results of Ta- and Ga-doped LLZO under constant current densities of (a) 0.1 A_{avg} cm^{-2} and (b) 0.5 A_{avg} cm^{-2}. Internal resistance over time according to discharge curves derived from Ohm's law at (c) 0.1 A_{avg} cm^{-2} and (d) 0.5 A_{avg} cm^{-2}.

$$Li_{22}Si_5 \rightarrow Li_{13}Si_4 \rightarrow Li_7Si_3 \rightarrow Li_{12}Si_7. \quad (4)$$

Note that $Li_{22}Si_5$ exhibits extreme moisture sensitivity, presenting significant handling challenges even in dry room conditions (relative humidity below 3%).[56,57] Consequently, this investigation employed $Li_{13}Si_4$ as the initial material for anode fabrication. Owing to the smaller quantity of the anode material compared with the cathode material, the observed plateaus correspond to the sequential phase transformations of $Li_{13}Si_4$ → Li_7Si_3 → $Li_{12}Si_7$.

The Ga-LLZO electrolyte cell exhibited an earlier voltage decline than the Ta-LLZO cell under both discharge conditions, resulting in consistently lower voltage values across all discharge regions. Furthermore, when considering the 1.4 V cutoff voltage,[61] the Ta-LLZO cell demonstrated 1.23 times longer discharge at a low current density and 1.04 times longer discharge at a high current density. This indicated superior discharge performance with 1.23- and 1.04-times higher unit cell energy density for Ta-LLZO compared with Ga-LLZO. More detailed numerical values are presented in Table 1. The extended plateaus observed for the Ta-LLZO cell suggest stable electrochemical reactions. These plateaus are maintained by minimising voltage drops, which depends on a continuous reaction between electrodes and Li^+ ions. This, in turn, relies on rapid ion transport through the electrolyte to deliver sufficient Li^+ ions to the electrode surface during discharge. From these results, we can infer that the use of Ta-LLZO leads to a lower overall cell resistance at 500 °C compared with that of Ga-LLZO.

The internal resistance of the cell can be calculated using the voltage differentials, which can be partially related to the ionic conductivity of the electrolytes. The internal resistance (R_t) was calculated using the current value (I) and difference between the OCV (V_{OC}) and closed-circuit voltage (V_{CC}), according to Ohm's law: $R_t = (V_{OC} - V_{CC})/I$. The internal resistance calculated over time, which is shown in Fig. 2(c) and (d), confirms that cells employing Ga-LLZO exhibit higher internal resistance under both discharge conditions. The divergence between the two cells becomes markedly pronounced beyond 2500 s in Fig. 2(c) and 500 s in Fig. 2(d). This conclusively demonstrates that when Ga-LLZO is utilised in thermal batteries operating at 500 °C, it delivers inferior performance to Ta-LLZO.

Notably, the performance gap between the two electrolytes narrowed under high-current-density conditions. This convergence suggests dopant-dependent electrolyte stability under dynamic operating conditions and implies opposing degradation pathways. The total discharge time was approximately 1 h under 0.1 A_{avg} cm^{-2}, whereas under 0.5 A_{avg} cm^{-2}, it marginally exceeded 10 min. This increase in current density reflects accelerated reaction kinetics and shortened exposure time to the battery operational environment, potentially mitigating the degradation processes that occur during prolonged high-temperature operation. Extended exposure time to other battery components, such as the FeS_2 cathode, Li–Si anode, and molten LK salt, at 500 °C may progressively destabilise Ga-LLZO. Conversely, the superior structural or interfacial stability of Ta-LLZO alleviates such degradation but is limited by accelerated electrochemical reaction kinetics under high current densities. The reasons for this unexpected performance reversal may include differences in interface stability at high temperatures, which induce an undesirable side reaction or temperature-dependent phase transformations within the doped LLZO structures.

3.3. Influence of Li–Si alloy anodes on ionic conductivity of doped LLZO solid electrolytes under thermal battery discharge conditions

The impact of Li–Si alloy anodes on the ionic conductivity of doped LLZO solid electrolytes was investigated under operating conditions of the thermal battery. The experimental approach involved direct contact between the Li–Si alloy and LLZO pellets

Table 1 Thermal battery discharge performance metrics of Ta- and Ga-doped LLZO at a cutoff voltage of 1.4 V under constant current densities of 0.1 and 0.5 A_{avg} cm^{-2}

Discharge condition	Dopant type	OCV at 0 s [V]	Discharge time [s]	Specific capacity [mA h g^{-1}]	Volumetric energy density of the unit cell [W h L^{-1}]	Mass energy density of the unit cell [W h kg^{-1}]
0.1 A_{avg} cm^{-2}	Ta-LLZO	1.92	2114	740.6	46.9	250
	Ga-LLZO	1.92	1713	600.2	37.8	201
0.5 A_{avg} cm^{-2}	Ta-LLZO	1.92	379	663.9	40.0	213
	Ga-LLZO	1.92	364	637.6	38.1	203

at 500 °C for 5 h to clarify the interfacial reactions and their effects on ionic transport properties, as illustrated in Fig. 3(a). Distinct visual differences were observed between the two LLZO variants upon disassembling the co-heated Li–Si and LLZO pellets. The Ta-LLZO pellet exhibited partial blackening, concentrated in the central region of the upper surface (non-contact side), while preserving its original ivory colouration at the periphery. In contrast, the Ga-LLZO pellet exhibited complete blackening across the entire upper surface, indicating a more extensive transformation. The observed blackening of the LLZO pellets is consistent with the findings of Tsai *et al.*, who observed similar surface discolouration when doped LLZO pellets were placed in contact with Li sources at 250 °C.[41] The discolouration process, which was significantly more pronounced and rapid in Ga-doped samples, was initiated at the surface that was directly in contact with the Li source and progressively extended into the bulk material. This phenomenon is attributed to Li metal infiltration along grain boundaries of the solid electrolyte, which created O vacancies and reduces the LLZO structure.[39,41,62] In the case of Ga-LLZO, with the existence of precipitated Ga, the alloying effect could accelerate this process, as Ga can readily form Li–Ga alloys and facilitate more aggressive Li propagation through the pellet.[38,39,41,62] The infiltrated metallic Li and Li–Ga alloys possess high electronic conductivity, potentially leading to short-circuit pathways when their propagation becomes extensive.[38,41,63]

Fig. 3(b) shows the Arrhenius plots of the ionic conductivity measurements for both types of LLZO pellets before and after heating with Li–Si alloy pellets. Interestingly, while the activation energies remained relatively constant for both materials after the heat-treatment process, significant changes in absolute conductivity values were observed. Ta-LLZO exhibited a moderate increase in ionic conductivity (2.32×10^{-4} to 2.86×10^{-4} S cm^{-1} at room temperature) following contact with the Li–Si alloy. This is attributed to the partial infiltration of Li-based alloys into the pellet structure, as evidenced by the localised blackening, which resulted from the reduction of LLZO.[38,39,41,62] This Li penetration significantly reduces the distance that Li ions must traverse through the electrolyte, thereby improving overall ionic transport. Excessive Li infiltration can lead to short circuiting, compromising the functionality of the electrolyte. Conversely, Ga-LLZO demonstrated a substantial decrease in ionic conductivity (7.14×10^{-4} to 3.29×10^{-4} S cm^{-1} at room temperature) post-contact. Furthermore, Ta-LLZO exhibited increasingly superior ionic conductivity to Ga-LLZO as the temperature increased, as demonstrated by their conductivities at 373 K: 1.54 10^{-3} S cm^{-1} and 2.40 10^{-3} S cm^{-1}, respectively. These findings align with the discharge test results shown in Fig. 2, where Ta-LLZO exhibits superior electrical performance to Ga-LLZO. Although Ga-LLZO may have also benefited from shortened Li^+-ion pathways, performance-degrading factors (*e.g.* structural instability and side reactions) may have played a more dominant role, given the complex interplay of factors governing ionic conductivity.

3.4. Microstructural and elemental distribution analysis of post-discharge LLZO disks

Fig. 4(a) and (b) show SEM images with the corresponding EDS elemental mapping of uniaxially pressed Ta- and Ga-LLZO pellets, respectively, without thermal treatment. These images of the pellet surfaces, captured at 10 000× magnification, confirm the comparable particle sizes, which were also observed *via* particle size distribution analysis (Fig. S2†), ensuring that subsequent differences in ionic conductivity stemmed solely from dopant effects rather than the initial powder morphology. The particle sizes of Ta- and Ga-LLZO powders at a cumulative volume fraction of 50% (D_{50}) were nearly identical, measuring 3.93 and 3.28 μm, respectively. EDS mapping indicated homogeneous distributions of all constituent elements throughout both pellet types, with no significant elemental segregation or abnormalities detected at this stage.

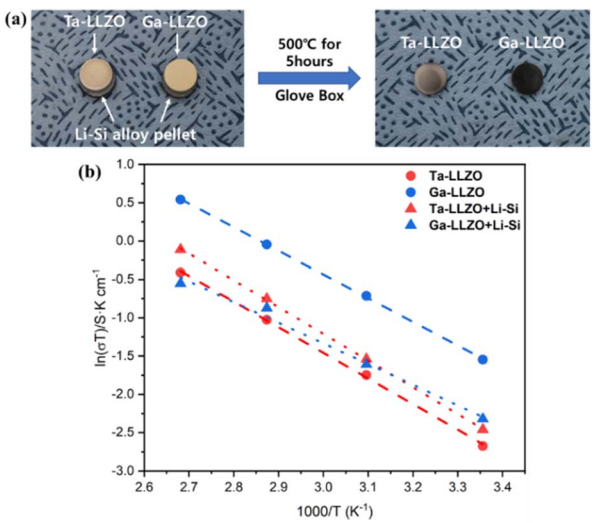

Fig. 3 (a) Photographs of the samples before and after heating; (b) Arrhenius plots of Ta- and Ga-doped LLZO in contact with the Li–Si alloy after being heated to 500 °C.

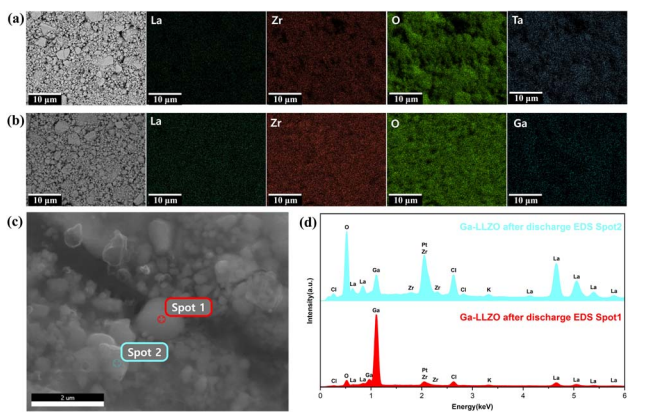

Fig. 4 Top-view SEM images with corresponding EDS elemental mapping of pristine (a) Ta-doped LLZO and (b) Ga-doped LLZO pellets. (c) Cross-sectional SEM image of Ga-doped LLZO disk after the thermal battery discharge test and (d) EDS spectra of Spots 1 and 2.

Table 2 Elemental compositions of Spots 1 and 2 obtained from EDS point analysis of Ga-doped LLZO disk after thermal battery discharge test

Element (at%)	O	Zr	Cl	La	Ga
Spot 1	40.41	3.60	4.66	3.92	47.41
Spot 2	78.05	6.34	4.92	9.40	1.29

Fig. 4(c) and (d) show the cross-sectional SEM images and EDS point analysis at 500 00× magnification. In the Ga-LLZO electrolyte disks, Ga-rich regions with 47.41 at% (Spot 1) were detected after completion of the full-cell assembly with LK salt and subsequent discharge testing. A more detailed elemental composition of Spots 1 and 2, obtained from the EDS point analysis, is presented in Table 2.

As the Ga-rich region was observed only after the discharge test, Ga precipitation is presumed to have occurred under high-temperature discharge conditions, probably owing to interfacial side reactions with other components of the thermal battery. The precipitated Ga is expected to exist primarily in the form of $LiGaO_2$, Ga_2O_3, and the Li–Ga alloy upon interaction with a Li source.[38,39,41,62,64] Although the present system utilised a Li–Si alloy rather than pure Li metal as the anode, Li–Si alloys exhibit sufficient reactivity to provide Li^+ ions and Li metal, which may induce similar degradation mechanisms. According to the findings of Windmüller *et al.* and Kim *et al.*, Ga-based oxides (*e.g.* Ga_2O_3) present at the interface can also react with Li^+ ions under discharge conditions, forming Li_2O and Li–Ga alloys.[62,63] Because oxides such as Ga_2O_3 and Li_2O typically possess low ionic conductivity, their formation at the interface can negatively impact the performance of the electrolyte. Moreover, the volume expansion accompanying oxide formation may lead to the development of microcracks in the solid electrolyte, further degrading the connectivity between particles and overall ionic conductivity.[38,39] This hypothesis could also account for the post-discharge observation that the Ga-LLZO disk fractured readily under minimal mechanical impact.

3.5. First-principles calculation for dopant precipitation

Fig. 5 illustrates the DFE of the bulk and interface structures of Ga- and Ta-LLZO. The DFE quantifies the energy required to release dopant species from either the bulk or interface regions. Overall, the interface presents a more energetically favorable configuration for dopant precipitation (release) compared to the bulk. With increasing temperature, the DFE decreased in both the Ga- and Ta-LLZO bulk structures, indicating enhanced dopant release at elevated temperature. At the LLZO–$Li_{13}Si_4$ interface, Ga-LLZO exhibits a decrease in DFE, whereas Ta-LLZO shows a significant rise, with the DFE shifting from negative to positive. This result indicates that at the elevated temperature of 773 K, Ga-dopant release remains thermodynamically favorable, whereas Ta-dopant release becomes unfavorable. This finding aligns with experimental observations of interfacial degradation described in Sections 3.3 and 3.4, where Ga-dopant

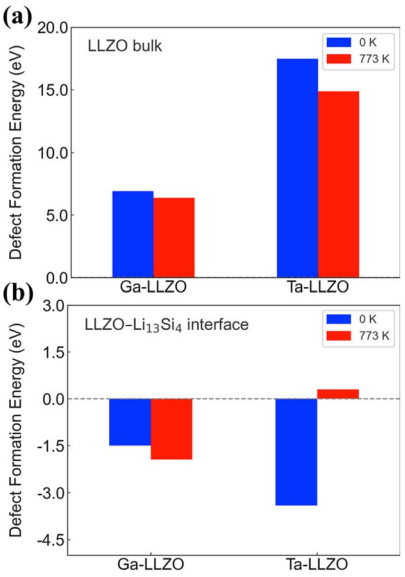

Fig. 5 DFE for Ga- and Ta-doped LLZO at 0 and 773 K. (a) LLZO bulk and (b) LLZO–$Li_{13}Si_4$ interfacial configuration.

segregation and related structural instability were observed in Ga-LLZO under the elevated-temperature condition.

In contrast, Ta-LLZO maintained its structural integrity, confirming its enhanced interfacial stability. The superior interfacial stability of Ta-LLZO compared with that of Ga-LLZO stems from the self-limiting nature of the "oxygen-deficient interphase" (ODI)-layer formation during reaction with Li sources. In Ta-LLZO, the ODI layer remains confined to an ultrathin thickness as Ta dopants exhibit minimal segregation to the interface, suppressing Zr^{4+} reduction.[65] The limited oxygen depletion may stabilize the bulk cubic phase, and suppress the phase transition to the tetragonal phase observed in Ga-LLZO. This enhanced electrochemical stability under operational conditions makes Ta-LLZO more suitable for practical applications in solid-state Li batteries where interface stability is paramount.

3.6. Phase evolution and structural stability of LLZO solid electrolytes at elevated temperatures

Fig. 6(a) and (b) present the *in situ* XRD patterns of pristine Ta- and Ga-LLZO samples, respectively, obtained at room temperature, 300 °C, 500 °C, and after cooling. The room-temperature (25 °C) patterns are consistent with those shown in Fig. 1(a). Despite being maintained at elevated temperatures of 300 and 500 °C for >1 h, neither Ta-LLZO nor Ga-LLZO exhibited significant structural transformations through significant changes in XRD patterns. The primary observable change was a marginal leftward shift of diffraction peaks with increasing temperature, which is attributed to the thermal expansion of the lattice parameters. Both doped LLZO variants displayed the emergence of $La_2Zr_2O_7$ (PDF# 17-450) impurity peaks at 500 °C, which persisted after cooling to room temperature, indicating an irreversible degradation process. The formation of $La_2Zr_2O_7$ in LLZO systems under harsh conditions has been reported in the literature, typically associated with Li volatilisation at

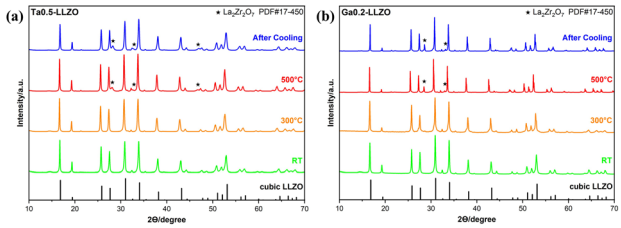

Fig. 6 *In situ* XRD patterns of pristine (a) Ta- and (b) Ga-doped LLZO powders.

elevated temperatures.[66,67] However, despite this secondary-phase formation, the primary sharp diffraction peak-based characteristic of the cubic LLZO structure remained intact, suggesting that the overall structural integrity of the bulk material was preserved.

Prior to investigating the interaction between doped LLZO and Li–Si alloy, the thermal stability of the Li–Si alloy was examined (Fig. S3†). At room temperature, the Li–Si alloy primarily exhibited $Li_{13}Si_4$ (PDF# 89-9) stoichiometry. With the increase in temperature, Li-deficient phases emerged, reflecting a continuous decrease in Li content. Concurrent with the diminishing Li–Si alloy signals, new diffraction peaks such as Li_2O (PDF# 65-2972), LiOH (PDF# 1-1021), Li_4SiO_4 (PDF# 19-727), and Li_2SiO_3 (PDF# 70-330) were observed, which resulted from reactions between trace amounts of oxygen/moisture and the Li–Si alloy.[68,69]

Fig. 7(a) and (b) show the *in situ* XRD patterns of Ta- and Ga-LLZO powders mixed with Li–Si alloy powder, subjected to the same thermal treatment protocol. The Ta-LLZO + Li–Si alloy mixture maintained remarkable structural stability, with no significant alterations to the primary LLZO structure. The newly formed peaks are attributed to either $La_2Zr_2O_7$ or the Li–Si alloy-derived impurities identified in the isolated Li–Si alloy study.

Conversely, the Ga-LLZO + Li–Si alloy mixture underwent structural transformations. The cubic LLZO structure, which remained stable up to 300 °C, transitioned predominantly to the tetragonal phase at 500 °C. This phase transformation may have been induced by the interaction between Ga-LLZO and the Li–Si alloy, resulting in Ga segregation in the LLZO structure and causing the lattice to revert from the cubic configuration to the tetragonal configuration.[38,39] Furthermore, the segregated Ga formed oxide compounds including Ga_2O_3 (PDF# 11-342), along with Li–Ga alloys such as LiGa (PDF# 65-9159) and Li_2Ga (PDF# 65-1383). The high-temperature-induced changes persisted after cooling, suggesting that the reaction was irreversible. Fig. 7(c) presents a magnified view of the 29–35° 2θ region shown in Fig. 7(b), allowing detailed peak analysis. Despite insignificant peak shifts relative to the tetragonal reference pattern, the breakdown of crystal symmetry associated with the cubic-to-tetragonal phase transition is clearly evident. Distinct Ga_2O_3 peaks emerged at 29.9° and 31.1° at 500 °C, confirming the decomposition of the Ga-LLZO structure when in contact with Li–Si alloy at elevated temperatures. The formation of these products is consistent with the predictions made according to the SEM/EDS analysis in Section 3.4.

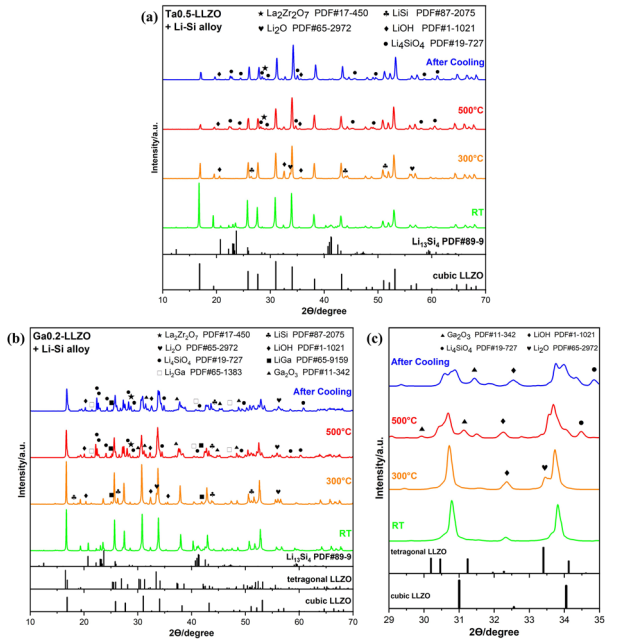

Fig. 7 *In situ* XRD patterns of the pristine (a) Ta-doped LLZO + Li–Si alloy mixture and (b) Ga-doped LLZO + Li–Si alloy mixture; (c) magnified view of the 29–35° 2θ region shown in (b).

The observed degradation of Ga-LLZO upon interaction with the Li–Si alloy at high temperatures exhibits detrimental effects on its electrochemical performance, particularly its ionic conductivity. Initially, upon exposure to the discharge environment, Ga was released from the lattice structure of Ga-LLZO owing to interfacial instability, as indicated by the DFE calculations. The leached-out Ga promotes rapid penetration of Li from the Li source into the bulk of the solid electrolyte *via* Li–Ga alloying, as evidenced by the prompt blackening of Ga-LLZO. This leads to a structural collapse from the cubic to tetragonal phase as Li captures oxygen atoms from the lattice. Under similar conditions, bandgap closure due to oxygen vacancies during this transition has also been reported in previous studies.[39,70] Moreover, $LiGaO_2$, which can form through the interaction of extracted oxygen and Ga during these processes, is expected to play a key role in the subsequent generation of impurities. $LiGaO_2$ can initiate a violent reaction when in contact with Li, generating Li–Ga alloys alongside oxides such as Li_2O and Ga_2O_3.[38,39,41,62,63] Thus, the conversion from the highly conductive cubic phase to the less-conductive tetragonal phase, coupled with the formation of poorly conducting oxide species, creates significant barriers to Li-ion transport. Moreover, the volume changes associated with these phase transformations and formation of secondary phases can induce microstructural cracking, further compromising the mechanical integrity and electrochemical functionality of the solid electrolyte.

3.7. Thermal stability and reactivity of doped LLZO solid electrolytes with thermal battery components

The thermal properties and potential reactions between doped LLZO solid electrolytes and various thermal battery components

were investigated using DSC. As shown in Fig. 6, LLZO garnet ceramics exhibit superior thermal stability at elevated temperatures.

Fig. 8(a) shows the DSC analysis results of Ta- and Ga-LLZO mixed with FeS_2 (cathode material). Regardless of the dopant type, both samples exhibited two endothermic peaks. A small peak appeared in the 400–420 °C range, whereas a larger peak spread across the 500–540 °C range. These peaks are attributed to the thermal decomposition of FeS_2, which exhibits similar endothermic peaks in these temperature ranges.[71] This suggests that the thermal events observed in the mixed samples were primarily due to inherent degradation of FeS_2 rather than reactions with the LLZO materials.

The DSC analysis results of Ta- and Ga-LLZO mixed with LK molten salt are presented in Fig. 8(b). Similar to the cathode mixture results, the two samples exhibit consistent thermal behaviour regardless of the dopant. A small endothermic peak is observed between 275 and 295 °C, followed by a stronger endothermic peak spanning the 310–360 °C range. The second larger peak is assigned to the melting of the LK eutectic salt, which has a reported melting point of 353 °C in a pure state.[72] However, in the presence of LLZO, the eutectic composition may be altered owing to surface chemical reactions. The LiCl–LiOH binary system exhibits melting within the temperature range of 269–292 °C at a composition of 32 mol% LiCl and 68 mol% LiOH.[73] When the LiOH that is formed on the LLZO surface combines with the LK molten salt, the eutectic point of the resulting ternary system (LiCl–KCl–LiOH) is lower than that of pure LK, producing the smaller endothermic peak.

Fig. 8(c) shows significant differences in thermal behaviour between different doped LLZO materials when mixed with the Li–Si alloy (anode material). Both samples exhibited a broad exothermic peak between 150 and 300 °C, which is attributed to the reaction of protonated LLZO that may have formed despite our moisture-control efforts.[74–76] Importantly, Ga-LLZO exhibited distinctly different thermal behaviour from Ta-LLZO at higher temperatures. Ga-LLZO exhibited a broad peak between 320 and 400 °C and a strong, intense peak above 500 °C. These peaks strongly suggest the occurrence of reactions between the doped LLZO materials and Li–Si alloy.

Cubic LLZO possesses high configurational entropy owing to its disordered Li^+ distribution, while the tetragonal phase adopts ordered Li^+ sites.[12,15,17,77] The spontaneous transition ($\Delta G < 0$) should be driven by a negative enthalpy change ($\Delta H < 0$) that compensates for the entropy loss ($\Delta S < 0$) associated with Li^+ sublattice ordering in the tetragonal phase. Therefore, the observed exothermic DSC peaks may correlate with the cubic-to-tetragonal phase transition of LLZO, as confirmed by *in situ* XRD at 500 °C (Fig. 7(b) and (c)).

Furthermore, the aforementioned reaction mechanism between Ga-LLZO and Li metal, where precipitated Ga forms $LiGaO_2$ or gallium oxides, subsequently reacting with Li to produce Li–Ga alloys and Li_2O, can be summarised as follows:[39]

$$LiGaO_2 + 5Li \rightarrow Li_2Ga + 2Li_2O. \quad (5)$$

The 0 K DFT calculations pertaining to the above reaction, as shown in Table S2,† confirm the exothermic nature of the solid-state process, with a negative reaction enthalpy of -41.4 kJ mol^{-1}, which may correspond to exothermic peaks observed in the high-temperature region of the DSC curves. This reaction involves the solid phases of $LiGaO_2$, Li, Li_2Ga, and Li_2O, as listed in the Materials Project database (data retrieved from the Materials Project for $LiGaO_2$ (mp-5854), Li (mp-135), Li_2Ga (mp-29210), and Li_2O (mp-1960) from database version v2025.04.10), which exhibit well-predicted lattice parameters with <4% deviation in volume.[78]

The DSC results clearly demonstrate that Ta-LLZO has superior thermal stability and compatibility with the Li–Si alloy compared to Ga-LLZO. Given these points, the diminished ionic conductivity in Ga-LLZO stems from multiple concurrent mechanisms that outweigh any beneficial effects of Li penetration: (1) structural transformation of the doped LLZO from the cubic phase to less-conductive tetragonal phase, (2) formation of various oxide species that impede ionic transport, and (3) substantial volume expansion leading to microcrack formation within the solid electrolyte. The competition between these enhancing and deteriorating mechanisms ultimately results in a net reduction of ionic conductivity for Ga-LLZO. This suggests that Ta-doped LLZO is the preferred choice for high-temperature solid-state battery applications where thermal stability and minimal reactivity with electrode materials are critical.

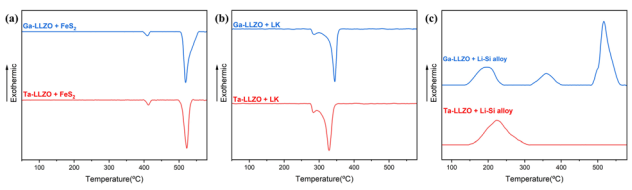

Fig. 8 DSC analysis of (a) Ta- and Ga-LLZO mixed with FeS_2, (b) Ta- and Ga-LLZO mixed with LK salt, and (c) Ta- and Ga-LLZO mixed with the Li–Si alloy.

4. Conclusions

Ta-LLZO garnet electrolytes outperformed Ga-doped variants in FeS_2/Li–Si thermal batteries under high-temperature operational conditions (500 °C), despite the superior room-temperature ionic conductivity of Ga-LLZO (7.14×10^{-4} S cm^{-1} *vs.* 2.32×10^{-4} S cm^{-1} for Ta-LLZO). At a current density of 0.1 A_{avg} cm^{-2}, Ta-LLZO cells exhibited 1.23 times higher specific capacity and 1.24 times higher energy density (both volumetric and mass). Although Ga^{3+} doping increased the Li^+ vacancy concentration, its interfacial instability with Li–Si anodes at high temperatures resulted in Ga precipitation, as verified by SEM/EDS analysis and first-principles calculations. Cubic-to-tetragonal phase transition and impurity formation led to conductivity loss during discharge according to *in situ* XRD and DSC results. Conversely, Ta^{5+} doping stabilised the cubic phase under thermal stress, resulting in stable discharge performance. The exothermic reactivity of Ga-LLZO with Li–Si

anodes, coupled with abnormal Li_2O/Ga_2O_3 formation, underscored its unsuitability for high-temperature applications. These findings emphasise that electrolyte selection for thermal batteries must prioritise high-temperature structural resilience and suggest that conventional room-temperature performance metrics may not translate directly to elevated-temperature operation. Future work will systematically explore co-doping and triple-doping strategies while optimising dopant ratios to maximise the electrical performance and interfacial stability of LLZO solid electrolytes for next-generation thermal batteries.

Data availability

The authors confirm that the data supporting the article have been included as part of the ESI.†

Author contributions

Hyungu Kang: writing – original draft, methodology, investigation, formal analysis, data curation. Heesook Roh: methodology, investigation, conceptualisation. Jongseo Lee: writing – review and editing, methodology, investigation, conceptualisation. Sang-Hyeon Park: writing – review and editing, investigation, data curation. Joohyeon Park: writing – original draft, investigation, data curation. Heonjae Jeong: writing – review and editing. Hyun-Ki Yoon: project administration, supervision. Tae-Young Ahn: writing – review and editing, methodology, investigation, conceptualisation, supervision. Yusong Choi: writing – review and editing, supervision.

Conflicts of interest

The authors declare that they have no known competing financial interest or personal relationships that could have appeared to influence the work reported in this paper.

Acknowledgements

This work was supported by Korean Government (Defense Acquisition Program Administration (DAPA)) in 2025 (915097102).

References

1 R. A. Guidotti and P. Masset, *J. Power Sources*, 2006, **161**, 1443–1449.
2 P. Masset and R. A. Guidotti, *J. Power Sources*, 2007, **164**, 397–414.
3 P. Masset, S. Schoeffert, J.-Y. Poinso and J.-C. Poignet, *J. Power Sources*, 2005, **139**, 356–365.
4 X. Liu, J. Liu, X. Liu, Z. Yang, H. Yu and F. Wang, *J. Electrochem. Soc.*, 2016, **163**, A617.
5 L. Schweiger, K. Hogrefe, B. Gadermaier, J. L. M. Rupp and H. M. R. Wilkening, *J. Am. Chem. Soc.*, 2022, **144**, 9597–9609.
6 N. Kamaya, K. Homma, Y. Yamakawa, M. Hirayama, R. Kanno, M. Yonemura, T. Kamiyama, Y. Kato, S. Hama and K. Kawamoto, *Nat. Mater.*, 2011, **10**, 682–686.
7 Z. Wu, X. Li, C. Zheng, Z. Fan, W. Zhang, H. Huang, Y. Gan, Y. Xia, X. He and X. Tao, *Electrochem. Energy Rev.*, 2023, **6**, 10.
8 D. A. Jokhakar, D. Puthusseri, P. Manikandan, Z. Li, J. Moon, H.-J. Weng and V. G. Pol, *Sustainable Energy Fuels*, 2020, **4**, 2229–2235.
9 Q. Xiao, C. Deng, Q. Wang, Q. Zhang, Y. Yue and S. Ren, *ACS Omega*, 2019, **4**, 95–103.
10 S. Yan, C.-H. Yim, V. Pankov, M. Bauer, E. Baranova, A. Weck, A. Merati and Y. Abu-Lebdeh, *Batteries*, 2021, **7**, 75.
11 Z. Zhang, X. Wang, X. Li, J. Zhao, G. Liu, W. Yu, X. Dong and J. Wang, *Mater. Today Sustain.*, 2023, **21**, 100316.
12 K. Eggestad, S. M. Selbach and B. A. Williamson, *J. Mater. Chem. A*, 2024, **12**, 15666–15675.
13 R. Murugan, V. Thangadurai and W. Weppner, *Angew. Chem., Int. Ed.*, 2007, **46**, 7778.
14 C. A. Geiger, E. Alekseev, B. Lazic, M. Fisch, T. Armbruster, R. Langner, M. Fechtelkord, N. Kim, T. Pettke and W. Weppner, *Inorg. Chem.*, 2011, **50**, 1089–1097.
15 G. Larraz, A. Orera and M. Sanjuán, *J. Mater. Chem. A*, 2013, **1**, 11419–11428.
16 J. Cai, B. Polzin, L. Fan, L. Yin, Y. Liang, X. Li, Q. Liu, S. E. Trask, Y. Liu and Y. Ren, *Mater. Today Energy*, 2021, **20**, 100669.
17 F. Chen, J. Li, Z. Huang, Y. Yang, Q. Shen and L. Zhang, *J. Phys. Chem. C*, 2018, **122**, 1963–1972.
18 H. Buschmann, S. Berendts, B. Mogwitz and J. Janek, *J. Power Sources*, 2012, **206**, 236–244.
19 Y. Zhou, X. Li, Y. Yang, X. Huang and B. Tian, *ACS Appl. Energy Mater.*, 2022, **5**, 13817–13828.
20 Y. Zhang, J. Deng, D. Hu, F. Chen, Q. Shen, L. Zhang and S. Dong, *Electrochim. Acta*, 2019, **296**, 823–829.
21 O. Sharifi, M. Golmohammad, M. Soozandeh and A. S. Mehranjani, *J. Solid State Electrochem.*, 2023, **27**, 2433–2444.
22 M. Aote, A. Deshpande, A. Khapekar and K. Parchake, *Mater. Lett.*, 2024, **377**, 137462.
23 J. Košir, S. Mousavihashemi, M. Suominen, A. Kobets, B. P. Wilson, E.-L. Rautama and T. Kallio, *Mater. Adv.*, 2024, **5**, 5260–5274.
24 L. Jun, W. Fuzhong, M. Leichao, G. Tao, B. Liang, H. Zhang, C. Meili, L. Xinxin, C. Ying and C. Jiyong, *Mater. Sci.*, 2024, **30**, 8–13.
25 S. Qin, X. Zhu, Y. Jiang, M. e. Ling, Z. Hu and J. Zhu, *Appl. Phys. Lett.*, 2018, **112**, 113901.
26 J. Li, J. Zhang, H. Zhai, X. Tang and G. Tan, *J. Eur. Ceram. Soc.*, 2022, **42**, 1568–1575.
27 C.-L. Tsai, S. Yu, H. Tempel, H. Kungl and R.-A. Eichel, *Mater. Technol.*, 2020, **35**, 656–674.
28 M. M. Raju, F. Altayran, M. Johnson, D. Wang and Q. Zhang, *Electrochem*, 2021, **2**, 390–414.
29 X. Huang, J. Su, Z. Song, T. Xiu, J. Jin, M. E. Badding and Z. Wen, *Ceram. Int.*, 2021, **47**, 2123–2130.
30 G. Kresse and J. Furthmüller, *Phys. Rev. B:Condens. Matter Mater. Phys.*, 1996, **54**, 11169–11186.
31 P. E. Blöchl, *Phys. Rev. B:Condens. Matter Mater. Phys.*, 1994, **50**, 17953–17979.

32 J. P. Perdew, K. Burke and M. Ernzerhof, *Phys. Rev. Lett.*, 1996, **77**, 3865–3868.
33 J. D. Pack and H. J. Monkhorst, *Phys. Rev. B*, 1977, **16**, 1748–1749.
34 V. Wang, N. Xu, J.-C. Liu, G. Tang and W.-T. Geng, *Comput. Phys. Commun.*, 2021, **267**, 108033.
35 P. G. Sundell, M. E. Björketun and G. Wahnström, *Phys. Rev. B:Condens. Matter Mater. Phys.*, 2006, **73**, 104112.
36 M. W. Chase Jr, *J. Phys. Chem. Ref. Data*, 1985, **14**, 1.
37 L. Rezazadeh, S. Hasheminia and Z. Khakpour, *Adv. Ceram. Prog.*, 2023, **9**, 16–23.
38 X. Cheng, Q. Yan, R. Yan, X. Pu, Y. Jiang, Y. Huang and X. Zhu, *ACS Appl. Mater. Interfaces*, 2023, **15**, 59534–59543.
39 J. Li, H. Luo, K. Liu, J. Zhang, H. Zhai, X. Su, J. Wu, X. Tang and G. Tan, *ACS Appl. Mater. Interfaces*, 2023, **15**, 7165–7174.
40 H. El Shinawi and J. Janek, *J. Power Sources*, 2013, **225**, 13–19.
41 C.-L. Tsai, N. T. T. Tran, R. Schierholz, Z. Liu, A. Windmüller, C.-a. Lin, Q. Xu, X. Lu, S. Yu, H. Tempel, H. Kungl, S.-k. Lin and R.-A. Eichel, *J. Mater. Chem. A*, 2022, **10**, 10998–11009.
42 S. Kim, J.-S. Kim, L. Miara, Y. Wang, S.-K. Jung, S. Y. Park, Z. Song, H. Kim, M. Badding and J. Chang, *Nat. Commun.*, 2022, **13**, 1883.
43 W. Choi, H.-C. Shin, J. M. Kim, J.-Y. Choi and W.-S. Yoon, *J. Electrochem. Sci. Technol.*, 2020, **11**, 1–13.
44 H. El-Shinawi, S. M. El-Dafrawy, M. Tarek, A. F. Molouk, E. J. Cussen and S. A. Cussen, *RSC Adv.*, 2024, **14**, 7557–7563.
45 K. Ma, B. Chen, C.-X. Li and V. Thangadurai, *J. Mater. Chem. A*, 2024, **12**, 3601–3615.
46 R. Samsinger, S. Schopf, J. Schuhmacher, P. Treis, M. Schneider, A. Roters and A. Kwade, *J. Electrochem. Soc.*, 2020, **167**, 120538.
47 L. Cheng, E. J. Crumlin, W. Chen, R. Qiao, H. Hou, S. F. Lux, V. Zorba, R. Russo, R. Kostecki and Z. Liu, *Phys. Chem. Chem. Phys.*, 2014, **16**, 18294–18300.
48 E. Zhao, F. Ma, Y. Guo and Y. Jin, *RSC Adv.*, 2016, **6**, 92579–92585.
49 X. Shen, Q. Zhang, T. Ning, T. Liu, Y. Luo, X. He, Z. Luo and A. Lu, *Mater. Today Chem.*, 2020, **18**, 100368.
50 X. Zhang, C. Wang, P. Yang, X. Zhang, W. Chen, J. Liu, Y. Cui, X. Liu and X. Li, *Phys. Chem. Chem. Phys.*, 2021, **23**, 196–203.
51 T. DuBeshter and J. Jorne, *J. Electrochem. Soc.*, 2017, **164**, E3539.
52 C. N. Im, C. Hun Choi, H. R. Yu, T. Y. Ahn, H. K. Yoon, J. Seong Yeo and J. H. Cho, *Batteries Supercaps*, 2021, **4**, 304–315.
53 Y. Choi, S. Cho and Y.-S. Lee, *J. Ind. Eng. Chem.*, 2014, **20**, 3584–3589.
54 J. Ko, S. H. Kang, H.-W. Cheong and Y. S. Yoon, *J. Korean Ceram. Soc.*, 2019, **56**, 233–255.
55 B. Perdue, C. A. Apblett, L. E. Johnson, E. Allcorn and J. C. Leonard, *Carbon Monofluoride Based High Voltage Thermal Battery Cathode*, Sandia National Lab.(SNL-NM), Albuquerque, NM (United States), 2018.
56 R. A. Guidotti and P. J. Masset, *J. Power Sources*, 2008, **183**, 388–398.
57 T.-Y. Ahn, H.-W. Cheong, S.-H. Kang, J.-I. Lee, M. Kim and Y. Choi, *RSC Adv.*, 2022, **12**, 21978–21981.
58 C. J. Wen and R. A. Huggins, *J. Solid State Chem.*, 1981, **37**, 271–278.
59 A. Azad, K. Bateman, M. Irvine, A. B. Naden, S. A. Dickson, R. I. Smith, R. K. Gover and J. T. Irvine, *J. Mater. Chem. A*, 2025, **13**, 14836–14845.
60 J.-H. Cho, C. N. Im, C. H. Choi, S.-h. Ha, H.-K. Yoon, Y. Choi and J. Bae, *Electrochim. Acta*, 2020, **353**, 136612.
61 S.-H. Kang, J. Lee, T.-U. Hur, H.-W. Cheong and J. Yi, *Int. J. Electrochem. Sci.*, 2016, **11**, 4371–4379.
62 D. Kim, M. H. Nguyen, S. H. Chun, J. Jeon, B.-K. Kim and S. Park, *Int. J. Energy Res.*, 2024, **2024**, 9050890.
63 A. Windmüller, K. Schaps, F. Zantis, A. Domgans, B. W. Taklu, T. Yang, C.-L. Tsai, R. Schierholz, S. Yu and H. Kungl, *ACS Appl. Mater. Interfaces*, 2024, **16**, 39181–39194.
64 S. Chen, J. Li, K. Liu, X. Sun, J. Wan, H. Zhai, X. Tang and G. Tan, *Chin. Phys. B*, 2024, **33**, 088203.
65 Y. Zhu, J. G. Connell, S. Tepavcevic, P. Zapol, R. Garcia-Mendez, N. J. Taylor, J. Sakamoto, B. J. Ingram, L. A. Curtiss and J. W. Freeland, *Adv. Energy Mater.*, 2019, **9**, 1803440.
66 S. T. Montoya, S. A. Shanto and R. A. Walker, *Crystals*, 2024, **14**, 795.
67 J. Košir, S. Mousavihashemi, B. P. Wilson, E.-L. Rautama and T. Kallio, *Solid State Ionics*, 2022, **380**, 115943.
68 X. Zhou, Z. Qi, Q. Liu, J. Tian, M. Liu, K. Dong and Z. Lei, *Front. Mater.*, 2021, **7**, 628233.
69 Y.-S. Su, K.-C. Hsiao, P. Sireesha and J.-Y. Huang, *Batteries*, 2022, **8**, 2.
70 J. Liu, T. Wang, J. Yu, S. Li, H. Ma and X. Liu, *Materials*, 2023, **16**, 2510.
71 H. Ning, Z. Liu, Y. Xie and H. Huang, *J. Electrochem. Soc.*, 2018, **165**, A1725.
72 M. del Rocío Rodríguez-Laguna, R. H. Garcia, T.-S. Yoo, S. T. Anderson, G. P. Horne and R. Gakhar, *J. Mol. Liq.*, 2025, **418**, 126706.
73 N. Hassan, M. Minakshi, J. Ruprecht, W. Y. H. Liew and Z.-T. Jiang, *Materials*, 2023, **16**, 1434.
74 E. Yi, W. Wang, J. Kieffer and R. M. Laine, *J. Power Sources*, 2017, **352**, 156–164.
75 L. Cheng, M. Liu, A. Mehta, H. Xin, F. Lin, K. Persson, G. Chen, E. J. Crumlin and M. Doeff, *ACS Appl. Energy Mater.*, 2018, **1**, 7244–7252.
76 R. Grissa, S. Payandeh, M. Heinz and C. Battaglia, *ACS Appl. Mater. Interfaces*, 2021, **13**, 14700–14709.
77 Y.-Y. Ting, R. Ye, E. Dashjav, Q. Ma, S. Taminato, D. Mori, N. Imanishi, M. Finsterbusch, M. H. Eikerling, O. Guillon, P. Kaghazchi and P. M. Kowalski, *Front. Energy Res.*, 2024, **12**, 1–12.
78 A. Jain, S. P. Ong, G. Hautier, W. Chen, W. D. Richards, S. Dacek, S. Cholia, D. Gunter, D. Skinner and G. Ceder, *APL Mater.*, 2013, **1**, 011002.